

Supplementary Information to:

Metal organic framework nanosheets-polymer composite materials for gas separation applications

Tania Rodenas^{1,†}, Ignacio Luz^{2,†}, Gonzalo Prieto^{3,†}, Beatriz Seoane¹, Hozanna Miro⁴, Avelino Corma², Freek Kapteijn¹, Francesc X. Llabrés i Xamena^{2,*} and Jorge Gascon^{1,*}

¹ Catalysis Engineering, ChemE, Delft University of Technology, Julianalaan 136, 2628 BL Delft, The Netherlands.

² Instituto de Tecnología Química, Universidad Politécnica de Valencia, Consejo Superior de Investigaciones Científicas, Av. de los Naranjos, s/n, 46022 Valencia, Spain.

³ Max Planck Insitut für Kohlenforschung, Kaiser Wilhelm Platz 1, 45470 Mülheim an der Ruhr, Germany.

⁴ Kavli Institute of Nanoscience, Delft University of Technology, Lorentzweg 1, 2628 CJ Delft, The Netherlands.

[†]These authors contributed equally to this work.

*Correspondence to: flabres@itq.upv.es, j.gascon@tudelft.nl

Overview.

1. Materials and Methods.

1.1. Materials synthesis.

1.2. Characterization methods.

1.3. Gas separation experiments.

2. Supplementary Figures.

3. Supplementary Tables.

4. Supplementary Videos.

1. Materials and Methods.

1.1. Materials synthesis

1.1.1. Synthesis of metal-organic-frameworks.

Chemicals

All chemicals were used as received, without further purification. $\text{Cu}(\text{NO}_3)_2 \cdot 3\text{H}_2\text{O}$, $\text{Zn}(\text{CH}_3\text{COO})_2 \cdot 2\text{H}_2\text{O}$, $\text{Co}(\text{CH}_3\text{COO})_2 \cdot 4\text{H}_2\text{O}$, 1,4-benzenedicarboxylic acid (H_2BDC), 1,4-naphthalenedicarboxylic acid (1,4- H_2NDC), 2,6-naphthalenedicarboxylic acid (2,6- H_2NDC) chloroform (CHCl_3), *N,N*-dimethylformamide (DMF) and acetonitrile (CH_3CN) were of analytical grade (Sigma-Aldrich). Polyimide (PI) Matrimid® 5218 (kindly supplied by Huntsman Advanced Materials) was degassed at 453 K overnight under vacuum to remove the adsorbed water.

Synthesis of bulk-type CuBDC MOF

Bulk-type copper 1,4-benzenedicarboxylate (CuBDC) MOF was synthesized following the hydrothermal synthesis described by Carson et al.^[1]. Thus, 1.053 g of $\text{Cu}(\text{NO}_3)_2 \cdot 3\text{H}_2\text{O}$ and 724 mg of 1,4-benzenedicarboxylic acid and 87 mL of *N,N*-dimethylformamide (DMF) were mixed in a 250 mL round-bottom flask and refluxed at 100 °C during 24 h. The resulting powder was collected by centrifugation at 8000 rpm and the solid was consecutively washed 3 times with DMF (20 mL each step) followed by 3 times washing with CHCl_3 (20 mL each step) in order to efficiently remove remaining linker molecules which might have remained occluded in the MOF pores after synthesis. Finally, the material was kept in CH_2Cl_2 until the synthesis of the composite materials.

Elemental analysis was used to confirm the molecular formula of the as-synthesized solid. The empirical formula for solvated $\text{Cu}(\text{BDC} \cdot \text{DMF})$ is $\text{C}_{11}\text{H}_{11}\text{CuNO}_5$ (Molecular weight $300.76 \text{ g} \cdot \text{mol}^{-1}$), which translates into wt-% of C 43.93, H 3.69, Cu 21.12, N 4.66. In accordance, the experimental wt-% were C 43.89, H 3.74, Cu 21.02, N 4.71.

Synthesis of CuBDC MOF nanosheets

A glass tube with 14 mm of inner diameter was used to synthesize MOF nanosheets. A linker solution composed of 30 mg of H_2BDC dissolved in a mixture of 2 mL of DMF and 1 mL of CH_3CN was poured to the tube bottom. Over this solution, a mixture of 1 mL of DMF and 1 mL of CH_3CN was carefully added to prevent premature mixing of the two solutions. Finally, a metal precursor solution composed of 30 mg of $\text{Cu}(\text{NO}_3)_2 \cdot 3\text{H}_2\text{O}$ dissolved in a mixture of 1 mL of DMF and 2 mL of CH_3CN was also carefully added to the tube as the top layer. After leaving the tube to react at 40 °C for 24 h in static conditions, the formation of a blue precipitate was observed at the bottom of the tube which was collected by centrifugation at 8000 rpm and consecutively washed 3 times with DMF (1 mL each step) followed by another 3 times with CHCl_3 (1 mL each step). The resulting material was left suspended in CH_2Cl_2 until the synthesis of the composite materials. Under these synthesis conditions, a 10 % MOF yield was obtained.

Elemental analysis was used to confirm the molecular formula of the as-synthesized solid. In agreement with the empirical formula for Cu(BDC·DMF) elemental analysis revealed weight contents (wt-%) of: C 44.17, H 3.98, Cu 20.93, N 4.53.

The same synthesis methodology was further applied upon modification of a number of synthesis parameters, i.e. by omitting the intermediate solvent layer, varying the synthesis temperature or replacing CH₃CN for alternative co-solvents.

Generalization of the nanosheet synthesis approach to other MOF structures

To investigate the scope of the MOF nanosheet synthesis strategy, the method was extended to other MOF structures by selecting alternative metal nodes and organic linker molecules.

Zinc 1,4-benzenedicarboxylate (ZnBDC) was synthesized by using Zn²⁺ as metal cation and 1,4-benzenedicarboxylate as organic ligand. A linker solution composed of 20 mg of H₂BDC dissolved in a mixture of 2 mL of DMF and 1 mL of CH₃CN was employed as bottom liquid layer, a mixture of 1 mL of DMF and 1 mL of CH₃CN was the spacer layer, while a solution of 10 mg Zn(CH₃COO)₂·2H₂O in 1 mL of DMF and 2 mL of CH₃CN was the top, metal-containing layer. Synthesis took place at 40 °C for 24 hours under static conditions. Finally, the solid product was recovered by centrifugation and thoroughly washed as described previously for CuBDC nanosheets. Under these synthesis conditions, a 41 % MOF yield was obtained.

Cobalt 1,4-benzenedicarboxylate (CoBDC) was synthesized by using Co²⁺ as metal cation and 1,4-benzenedicarboxylate as organic ligand. A linker solution composed of 10 mg of H₂BDC dissolved in a mixture of 2 mL of DMF and 1 mL of CH₃CN was employed as bottom liquid layer, a mixture of 1 mL of DMF and 1 mL of CH₃CN was the spacer layer, while a solution of 10 mg Co(CH₃COO)₂·4H₂O in 1 mL of DMF and 2 mL of CH₃CN was the top, metal-containing layer. Synthesis took place at 25 °C for 24 hours under static conditions. Finally, the solid product was recovered by centrifugation and thoroughly washed as described previously. Under these synthesis conditions, a 56 % MOF yield was obtained.

Copper 1,4-naphthalenedicarboxylate (Cu(1,4-NDC)) was synthesized by using Cu²⁺ as metal cation and 1,4-naphthalenedicarboxylate as organic ligand. A linker solution composed of 30 mg of H₂NDC dissolved in a mixture of 2 mL of DMF and 1 mL of CH₃CN was employed as bottom liquid layer, a mixture of 1 mL of DMF and 1 mL of CH₃CN was the spacer layer, while a solution of 10 mg Cu(NO₃)₂·3H₂O in 1 mL of DMF and 2 mL of CH₃CN was the top, metal-containing layer. Synthesis took place at 60 °C for 24 hours under static conditions. Finally, the solid product was recovered by centrifugation and thoroughly washed as described previously. Under these synthesis conditions, a 70 % MOF yield was obtained.

Copper 2,6-naphthalenedicarboxylate (Cu(2,6-NDC)) was synthesized by using Cu²⁺ as metal cation and 2,6-naphthalenedicarboxylate as organic ligand. A linker solution composed of 10 mg of H₂NDC dissolved in a mixture of 2 mL of DMF and 1 mL of CH₃CN was employed as bottom liquid layer, a mixture of 1 mL of DMF and 1 mL of CH₃CN was the spacer layer, while a solution of 10 mg

$\text{Cu}(\text{NO}_3)_2 \cdot 3\text{H}_2\text{O}$ in 1 mL of DMF and 2 mL of CH_3CN was the top, metal-containing layer. Synthesis took place at 40 °C for 24 hours under static conditions. Finally, the solid product was recovered by centrifugation and thoroughly washed as described previously. Under these synthesis conditions, a 75 % MOF yield was obtained.

1.1.2. Synthesis of MOF-polymer composite materials and membrane casting.

To prepare the MOF-polymer composite materials, the MOF crystals or nanosheets were dispersed in chloroform and ultrasonicated (power=50 W and frequency= 60 Hz) for 1 hour. Then the polymer Matrimid 5218 (0.4 g), previously degassed at 180 °C overnight under vacuum to remove the adsorbed water, was stepwise added to the MOF suspension in two portions of 0.2 g, to obtain a final mass ratio solvent/(MOF+polymer) of 90/10. The resulting suspensions were gently shaken for 12 hours in a laboratory shaker (5.3 Hz) at room temperature. The MOF/polymer mass ratio was selected to achieve the desired final MOF loading in the composite materials.

Before the casting of the thin membranes, three cycles were carried out each consisting of dispersing the suspension of MOF and polymer in an ultrasounds bath for 15 minutes, followed by shaking for 30 minutes. Afterwards, the viscous suspension was poured on a flat surface and shaped as a thin film under shear forces by a doctor Blade knife. Next, the solvent was removed by evaporation, first by natural convection at room temperature for 8 hours, followed by a treatment in a vacuum oven (75 torr) at 180 °C for 12 h. This temperature was selected below the glass transition temperature (T_g) of the polymer (317 °C) to prevent the transition into a rubbery-state. The final thickness of the resulting composite films was evaluated using a digital micrometer (Mitutoyo, Quickmike Series). For reference purposes, neat polymer membranes were prepared following an identical procedure without MOF incorporation.

1.2. Characterization methods.

1.2.1. Elemental analysis.

Elemental analysis was performed on the dried, as-synthesized MOFs in a Fisons EA1108 instrument using sulphanilamide as standard.

1.2.2. X-ray diffraction.

X-ray diffraction was used to study the crystalline structure of the MOF materials. XRD patterns were recorded using a Phillips X'Pert diffractometer with Cu $K\alpha$ radiation ($\lambda=1.54778 \text{ \AA}$) or a Bruker D8 Advanced diffractometer with Co $K\alpha$ radiation ($\lambda=1.78897 \text{ \AA}$). The samples were scanned using a *step size* of 0.02-0.04° and a *scanspeed* of 1 s per step in a continuous scanning mode. Bulk MOF specimens were prepared by filling the holder with the dry powder. In the case of MOF nanosheets, the specimen was prepared by slow evaporation of a couple of drops from a suspension of the material in dichloromethane over a zero-background single-crystal silicon sample holder.

1.2.3. Scanning Electron Microscopy (SEM).

SEM experiments were conducted in a Zeiss ULTRA 55 microscope equipped with a Field-Emission (FE) electron beam source with 1 nm SEM imaging resolution and operated at an accelerating voltage of 0.5 kV. Bulk MOF specimens were prepared by applying the dry powder directly on the sample holder. In the case of MOF nanosheets, a couple of drops from a suspension of the material in dichloromethane were applied and let dry over the sample holder. To acquire the FE-SEM images shown, it was not necessary to sputter the specimens with any conductive layer.

1.2.4. Atomic Force Microscopy (AFM).

AFM micrographs were recorded with a Veeco Multimode Nanoscope 3A microscope operating in tapping mode. The MOF samples were applied to a previous annealed mica wafer substrate. Before microscopy inspection, a couple of drops from a suspension of MOF nanosheets in dichloromethane were applied and let dry over the mica substrate.

1.2.5. Transmission Electron Microscopy (TEM).

Transmission electron microscopy (TEM) experiments were performed in a JEOL JEM-1010 microscope operated a 100 kV. Before TEM observation, the specimens were prepared by applying a few drops of the MOF chloroformic suspensions on a carbon-coated copper grid and letting it dry.

1.2.6. Thermogravimetric analysis (TGA).

TGA was applied to determine the MOF content in the MOF-polymer composites. The experiments were performed in a Mettler Toledo TGA/SDTA851e apparatus by heating the sample from room temperature to 1123 K at a rate of 10 K·min⁻¹ in flow of synthetic air (60 mL·min⁻¹). The MOF content was derived from the mass of the residual CuO after complete combustion.

1.2.7. Gas sorption isotherms.

Sorption isotherms of the MOF materials were determined with N₂ (at 77 K), Ar (at 87 K), CO₂ and CH₄ (at 298 K) adsorbates in a Tristar II 3020 Micromeritics equipment. Prior to the measurements, the adsorbent was outgassed at 453 K under dynamic vacuum for 16 hours.

1.2.8. FIB-SEM tomography.

Serial sectioning and micrograph acquisition

Focused Ion Beam-Scanning Electron Microscopy (FIB-SEM) experiments were performed in a DualBeam Strata 235 microscope (FEI) and an AURIGA Compact (Zeiss) microscope. The membranes were first sputter coated with a ca. 20 nm Au layer. Before milling, a protective layer of Pt (0.3 μm thickness) was deposited on the areas of interest of the specimen using the gas injection system. Then, the Ga⁺ FIB, working at 30 kV and 20·10³ pA, was used to create a ca. 20 μm-wide trench on the top

surface of the membranes. Serial sectioning combined with SEM imaging was carried out using an automated routine programmed in RunScript software with drift correction. Slices with nominal thickness of 52 nm were milled away by the FIB, operating at 30 kV and $7 \cdot 10^3$ pA. Between 124 and 150 individual SEM micrographs of the consecutive cross-sections exposed upon milling were recorded, at magnifications of 12000-25000, with a Secondary Electron Detector in the SEM operated at 5 kV.

Dataset processing and tomogram reconstruction

The collection of consecutive SEM micrographs was processed to reconstruct the 3D internal structure of the membranes. The stack of images was aligned to an external feature on the membrane surface using a cross-correlation algorithm. A central region of the FIB-exposed face of the trench was selected and cropped for further analysis. Next, a stretching operation in the y-direction was performed to correct the foreshortening caused by the tilt angle between the specimen cross-section and the SEM detector. A bandpass filter was applied to the resulting aligned stack to reduce shadowing effects by the trench walls as well as vertical curtaining, followed by mean-field filtering (with a circular kernel) to enhance the contrast of the embedded MOF particles relative to the polymeric matrix, and thereby facilitate subsequent image segmentation. The final 3D reconstructions displayed non-cubic voxels with $x:y:z$ dimensions of (11.8-24.5):(11.8-24.5):52 nm.

Tomogram segmentation and image analysis

To quantify parameters of interest from the reconstructed FIB-SEM tomograms, segmentation of the different phases, i.e. polymer matrix, MOF particles and internal voids, was performed in Avizo (FEI Visualization Sciences Group). A contrast mask was applied to the aligned stack of SEM micrographs to identify 3D connected regions with contrast levels between manually selected thresholds. As a result of the inherent overall contrast variations in sequential SEM imaging and remaining curtaining effects, the accurate segmentation of the ultrathin MOF nanosheets required adjustments of the automatically recognized volumes with controlled erosion-dilation functions and manual adjustments. An isosurface rendering process was applied to compute triangular approximations of the interfaces between the different phases. This allowed quantification of the MOF surface area. 3D-surface rendered views of the segmented tomograms were generated with a constrained smoothing of the MOF particles, representing the polymer matrix as a fully transparent phase.

The MOF weight content in the volumes studied with FIB-SEM tomography was determined from the corresponding volumes for the segmented phases. A density of 1.24 g cm^{-3} was employed for the polyimide matrix, while the crystallographic density of 1.66 g cm^{-3} was considered for the CuBDC MOF. The density of the internal voids was considered negligible. In all cases, the MOF loading from image analysis was in agreement with the overall content. As an example, MOF loadings of 8.50 and 7.03 wt% were determined by image analysis of the tomograms for *b*-CuBDC(8)@PI and *ns*-CuBDC(8)@PI composite materials depicted in Figure 4 (main article). These values are in fairly good correspondence with the overall MOF content of the membranes as determined by thermogravimetric analysis: 7.9 and 8.2 wt% for *b*-CuBDC@PI and *ns*-CuBDC@PI, respectively. These results confirm that the regions examined with FIB-SEM are representative and allow a direct comparison of the structures determined for both composite membranes at a similar MOF content level. The negative

deviation of the MOF loading determined for *ns*-CuBDC(8)@PI by image analysis with respect to the overall MOF content might arise from the presence of few very thin MOF lamellae, which are not detected as their thickness falls below the imaging resolution. Very low void volume fractions were determined for both composites, i.e. 0.06% and 0.12% for *b*-CuBDC(8)@PI and *ns*-CuBDC(8)@PI, respectively.

Further image quantification involved the analysis of the occupation by the MOF particles of the membrane *xz* cross-section perpendicular to the gas flux (when applied in gas separations). As the gas flux direction, i.e. the direction of the pressure gradient established between the two sides of the membranes during the gas permeation experiments (*y*-axis in the tomograms) is perpendicular to the FIB-milling direction employed to record the raw data, the analysis required the generation of a collection of virtual cross-sections through the segmented tomograms along the *y*-axis. A resolution of ten times the voxel size in the *y*-direction was considered adequate. Hence, groups of 10 single-voxel-thick virtual cross-sections were merged and projected on a single plane. The percentage of cross-section occupied by the MOF particles was determined by quantifying the number of pixels corresponding to MOF out of the total projected cross-section. This analysis was performed individually for several cross-sections at increasing depth levels over the entire height of the tomograms. The cumulative MOF cross-section coverage, again as a function of the analysis depth in the *y* direction, was determined in a similar manner, generating cumulative projections on a single plane to account for (partial) vertical overlap of MOF particles.

The 3D orientation of the MOF nanosheets in the *ns*-CuBDC(8)@PI composite membrane was also quantified with image analysis. This analysis involved a population of 150 randomly selected lamellae contained in the reconstructed volume. For each lamella, the 3D coordinates were determined of three points in space, which defined a plane representing its orientation. These three points corresponded to centers of voxels located at the center of mass of the sheet (p_1) and two opposite vertices of the sheet (p_2 and p_3). Then, the equations of the vectors v_1 (going from p_1 to p_2) and v_2 (going from p_2 to p_3) were determined from the coordinates of the selected points. Next, the equation of the vector normal to the nanosheet plane (v_n) was calculated as the cross product of vectors v_1 and v_2 (equation (1)).

$$v_n = v_1 \times v_2 \quad \text{eq. (1)}$$

The angle formed by the sheet with the *y*-axis was determined as given in equation (2):

$$\alpha = \arccos \left[\frac{v_n \cdot v_y}{|v_n| \cdot |v_y|} \right] \quad \text{eq. (2)}$$

where α is the angle formed by the sheet plane with the *y*-axis in 3D space, and v_y is the vector defining the direction of the *y*-axis, i.e. (0 1 0).

From the value of α , the efficiency with which each nanosheet covered the membrane cross-section perpendicular to the gas flux was determined as the ratio between the sheet area projected on the *xz* plane (A_{proj}) and the actual area of the sheet (A_{lam}), (equation (3)).

$$\eta = \cos(\pi/2 - \alpha) \cdot 100 \text{ (\%)} \quad \text{eq. (3)}$$

where η is the coverage efficiency of a single lamella and α is the angle formed by the nanosheet plane with the y -axis.

1.3. Gas permeation experiments.

Membrane areas of 4.4 cm² were cut from the casted films, placed on a macroporous support and mounted in a flange between Viton O-rings. This flange fit in a permeation module which was placed inside an oven in a permeation setup described elsewhere^[2]. An equimolar mixture of CO₂ and CH₄ (100 mL·min⁻¹ total flow rate) was employed as gas feed. Helium (67.7 mL·min⁻¹) was used as sweep gas for the permeate stream, while the trans-membrane pressure was adjusted using a backpressure controller at the retentate side. An on-line gas chromatograph equipped with a packed Carboxen 1010 PLOT (30 m × 0.32 mm) column and TCD and FID detectors was used to periodically analyze the permeate stream.

Gas separation performance was defined by the separation selectivity and the gas permeabilities (P) of the individual components.

The permeability for the j -component (P_j) was calculated as shown in equation (4):

$$P_j = \frac{\varphi_{n,j} \cdot \delta}{\Delta P_j \cdot A} \quad \text{eq. (4)}$$

where $\varphi_{n,j}$ denotes the molar flow rate of j -component, δ is the thickness of the membrane, ΔP_j is the partial pressure difference of the j -component across the membrane and A is the membrane area.

The SI unit for the permeability is mol·s⁻¹·m⁻¹·Pa⁻¹. However, here gas permeabilities are reported in the widely used non-SI unit *Barrer*, where 1 *Barrer* = 3.35·10⁻¹⁶ mol·m⁻¹·Pa⁻¹·s⁻¹. The separation factor or mixed gas selectivity (α) was calculated as the ratio of the permeability of the more permeable compound (CO₂) to the permeability of the less permeable compound (CH₄) as given in equation (5).

$$\alpha = \frac{P_{CO_2}}{P_{CH_4}} \quad \text{eq. (5)}$$

2. Supplementary Figures.

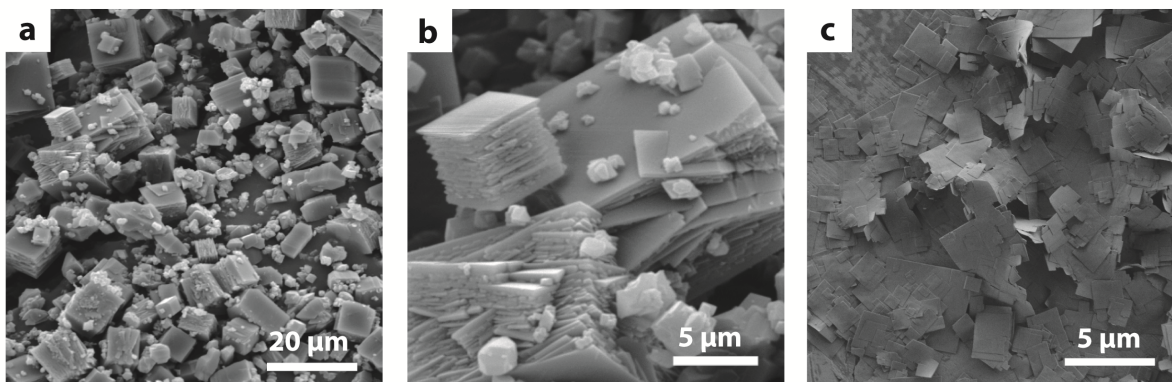


Figure S1. Scanning electron microscopy analysis of as-synthesized **a,b**, *bulk-like* and **c**, nanosheet CuBDC MOF crystals.

Fig. S1 shows overview SEM micrographs of CuBDC MOF with different crystal morphologies. CuBDC MOF crystals obtained by the conventional solvothermal method uniformly display a cubic morphology with edge lengths mainly spanning in the 2-10 μm range (Fig. S1a,b). For CuBDC MOF nanosheets, Fig. S1c evidences the absence of bulk-like crystals. In contrast, well-defined square lamellae with lateral dimensions ranging in 0.5-4 μm are observed, indicating that the multi-layer synthesis strategy employed to produce MOF nanosheets not only dramatically limits the crystal dimensions in the stacking direction but it also reduces MOF growth in the basal directions.

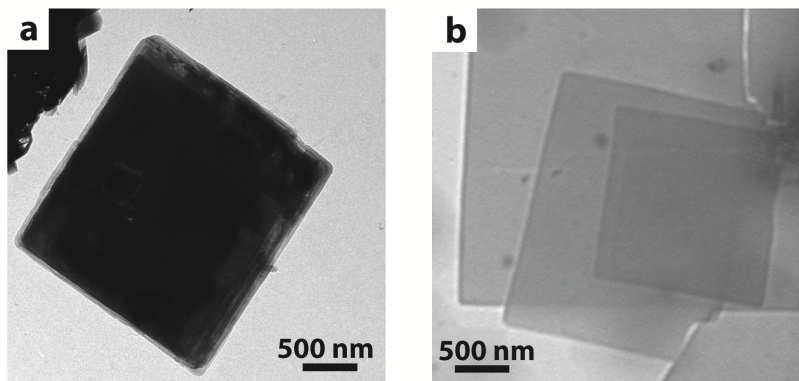


Figure S2. Representative transmission electron micrographs of **a**, CuBDC MOF crystals obtained by a conventional solvothermal method, and **b**, CuBDC nanosheets produced by the multi-layer synthesis strategy.

Transmission electron microscopy revealed that the MOF nanosheets display a very regular morphology, with well-defined edges and an intact internal structure.

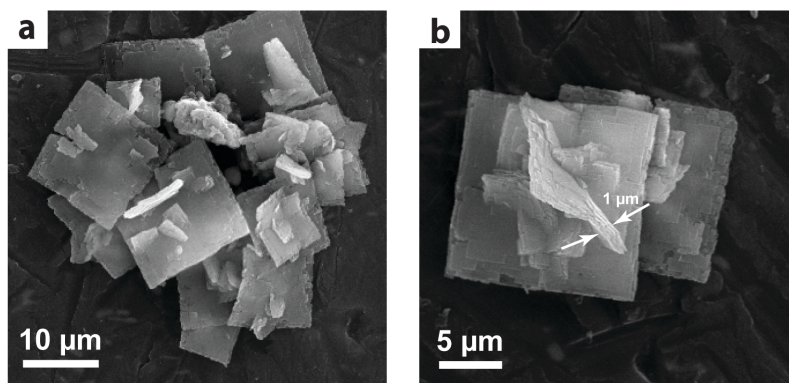


Figure S3: Scanning electron micrographs, at different magnifications, of CuBDC crystals synthesized at 313 K, upon modification of the three-layer methodology by omission of the intermediate solvent spacer layer.

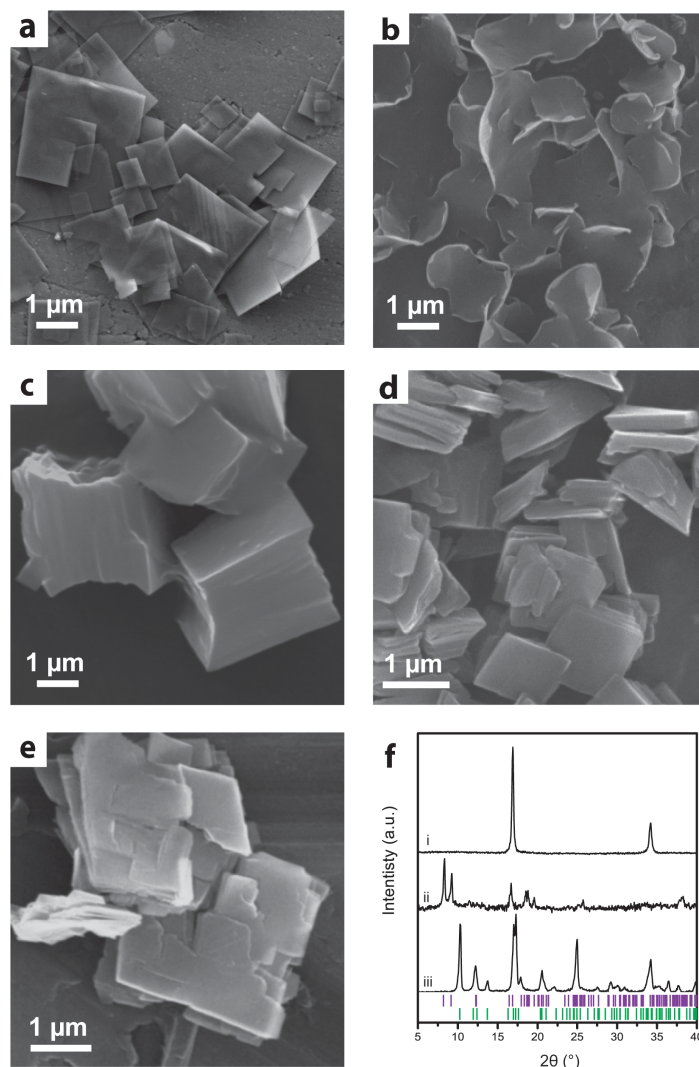


Figure S4: Scanning electron micrographs of CuBDC MOF crystals synthesized at 313 K via the three-layer approach using **a**, acetonitrile, **b**, propionitrile, **c**, methanol, **d**, 2-propanol and **e**, acetone as spacer solvent. Panel **f** displays the X-ray diffraction patterns (Cu K α radiation) of the solids synthesized with the different co-solvents. From top to bottom: acetonitrile (i), isopropanol (ii) and acetone (iii). The set of green (bottom) and purple (top) short tick marks underneath the patterns indicate the position of diffraction lines expected for the solvated CuBDC·DMF (Monoclinic, space group $C2/m$, $a = 11.414$, $b = 14.269$, $c = 7.780$, $\beta = 108.12^\circ$) and desolvated CuBDC (Triclinic, $P-1$, $a = 5.25$ Å, $b = 9.67$ Å, $c = 10.77$ Å, $\alpha = 90.29^\circ$, $\beta = 91.06^\circ$, $\gamma = 92.413^\circ$), respectively.

The nature of the co-solvent/spacer employed in the three-layer methodology was found to influence the crystal morphology and the crystalline structure of the obtained CuBDC MOF crystals. Acetonitrile and propionitrile afforded very high aspect ratio nanosheet crystals whose crystalline structure corresponds to that expected for the as-synthesized, layered CuBDC·DMF MOF with a very strong preferential orientation along the basal plane of the lamellae (in the $[\bar{2}01]$ direction)^[1]. However, while the nanosheets displayed well-defined orthogonal edges in the case of acetonitrile, the use of propionitrile resulted in notably rounded edges, indicative of an effect of the spacer co-solvent on the crystal growth behavior along the basal plane. Using alcohols as spacer solvents led to crystals with a significantly

reduced aspect ratio. The CuBDC crystals consisted of micron-sized cubes in the case of methanol, similar in size and aspect-ratio to the bulk-type crystals obtained under conventional solvothermal conditions. The use of a less polar alcohol such as 2-propanol resulted in a slight increase in the aspect ratio owing to sub-micron crystal thicknesses along the stacking direction. Moreover, the use of alcohol as co-solvent leads to materials having XRD patterns analogous to that described for desolvated CuBDC^[3]. Note in particular the presence of two diffraction peaks at 8.35° and 9.33° 2θ (with Cu $K\alpha$ radiation), which are totally absent in the layered solvated structure. This desolvated material is typically formed from the layered structure upon removal of the *N,N*,dimethylformamide (DMF) molecules coordinated to the apical position of both Cu ions in the paddle-wheel units and formation of new interlayer Cu-O bonds between copper ions in one layer and oxygen atoms in the adjacent layers. When alcohols are employed as co-solvent, stronger adsorption on the metal nodes leads to displacement of the DMF solvation molecules, facilitating the formation of the 3D crystalline structure, in line with very recent results by Carson et al.^[3]. Use of acetone as co-solvent spacer led to platelet crystals with sub-100 nm thickness, hence with intermediate aspect ratios between those obtained with nitrile and alcohol solvents. The XRD pattern of this material corresponds to the layered CuBDC·DMF structure, while the detection of several diffraction lines is in agreement with a lower preferential growth compared to the ultrathin nanosheet crystals obtained with acetonitrile or propionitrile as spacer co-solvents.

Such large differences in crystal morphology and crystalline structure can hardly be explained by the small density differences of the various co-solvents used (between 0.786 and 0.792 cm³/g) with respect to DMF (0.944 cm³/g). Other properties of the solvent (e.g., polarity) are also relevant for controlling crystal growth and thereby the final morphology and structure of CuBDC crystals. The mechanism underlying the different growth modes seems at least partially related to the different coordination strengths of the solvent molecules to Cu₂ paddle-wheel units, thus affecting the stacking of the 2D layers and the tendency to transform into the desolvated structure. Modulation of the kinetics of deprotonation of the benzene dicarboxylic acid in different solvents may also affect crystal growth rate and morphology. While alcohols facilitate the formation of bulkier crystals of a compact 3D framework via interference with DMF solvation of the metal nodes, polar aprotic solvents are preferred to accomplish high-aspect-ratio nanocrystals of the CuBDC·DMF framework. In addition, our results highlight the possibility to control the morphology and aspect ratio of CuBDC·DMF nanosheet/platelet crystals via judicious selection of the solvent in the buffer layer, expanding the scope of this synthesis route.

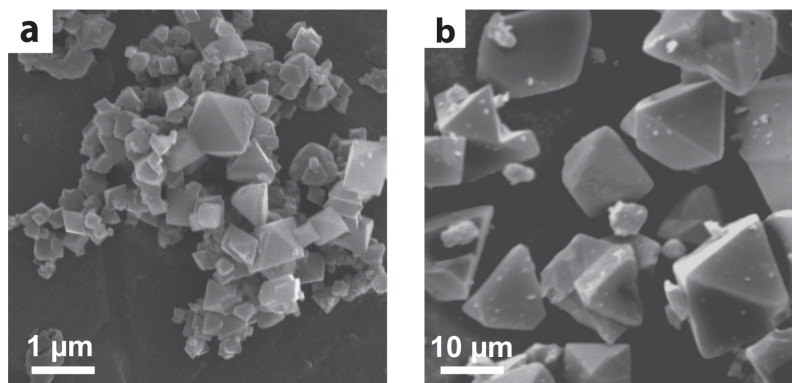


Figure S5: Scanning electron micrographs of Cu(BTC), or HKUST-1, MOF synthesized via **a**, the three-layer methodology and **b**, a conventional solvothermal route^[4].

The tridimensional metal organic framework Cu(BTC), or HKUST-1^[5], shows a natural propensity to a 3D crystal growth mode. As observed in the micrographs above, the application of the three-layer synthesis strategy to this MOF renders primarily octahedral shaped crystals, with morphologies and aspect ratios similar to those achieved via a more conventional solvothermal route, though with notably smaller crystal size.

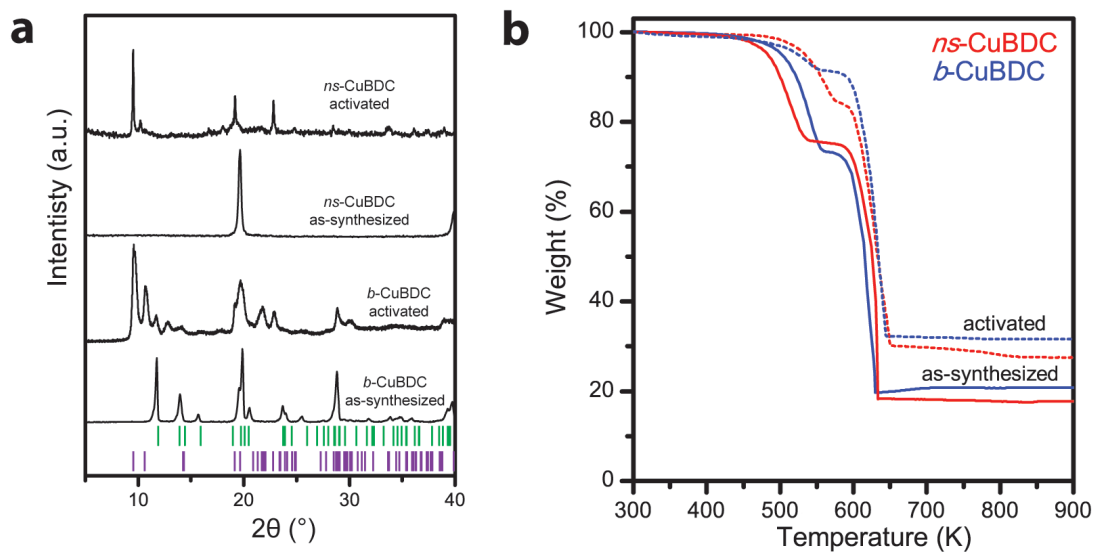


Figure S6. a, X-ray diffraction patterns (CoK α radiation) for bulk-type and nanosheet CuBDC MOFs, as-synthesized and after the activation treatment. Green and purple lines indicate the position of diffraction lines expected for the solvated CuBDC·DMF (Monoclinic, space group $C2/m$, $a = 11.414$, $b = 14.269$, $c = 7.780$, $\beta = 108.12^\circ$) and desolvated CuBDC (Triclinic, $P-1$, $a = 5.25$ Å, $b = 9.67$ Å, $c = 10.77$ Å, $\alpha = 90.29^\circ$, $\beta = 91.06^\circ$, $\gamma = 92.413^\circ$), respectively; **b**, thermogravimetric profiles for bulk-type (blue) and nanosheet (red) CuBDC MOFs, as-synthesized (full lines) and after the activation treatment (dotted lines).

X-ray diffraction analysis after activation demonstrated retention of crystallinity for CuBDC, irrespective of whether in bulky or nanosheet crystals. In both cases, development of the structure corresponding to the desolvated CuBDC framework was observed, in agreement with previous reports on this MOF^[1]. Thermogravimetric analysis showed a weight loss of 24-27 % in the temperature range of 453-573 K for the as-synthesized CuBDC·DMF MOFs, corresponding to the release of ca. 1 molecule of DMF per Cu atom. After activation, TGA demonstrated the removal of a significant fraction of the solvate molecules, remaining <0.5 DMF molecules per Cu atom in the activated materials. The results indicate that similar activation degrees were achieved for both MOF crystal morphologies.

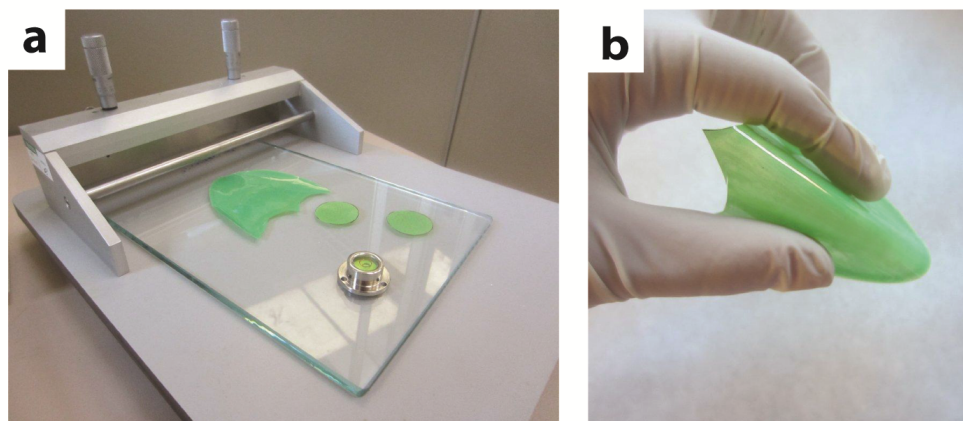


Figure S7. Illustration of the casting of MOF-polymer composite materials as ultrathin membranes. Panel **a** depicts the Doctor Blade device employed to cast the membranes. Circular membrane pieces cut out to be used in the gas permeation experiments are also displayed. Panel **b** shows a flexible composite membrane with a thickness of ca. 30 μm .

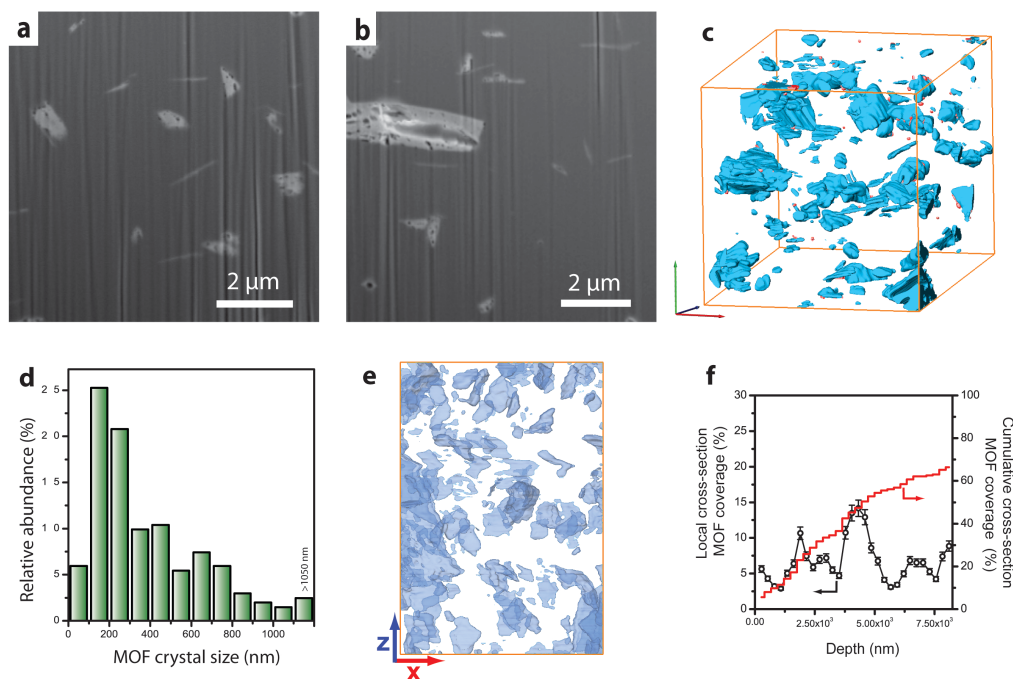


Figure S8: Structural characterization of *nc*-CuBDC(8)@PI, incorporating CuBDC nanocrystals, obtained via the three-layer synthesis approach at 333 K. **a,b, SEM micrographs of cross-sections of the composite membrane exposed via FIB milling. **c**, 3D surface-rendered view of the segmented FIB-SEM tomogram of the composite (MOF in blue and voids in red). **d**, MOF particle size distribution (longest axis) as derived from image analysis of the FIB-SEM tomogram. **e**, Full projection along the y (gas flux) direction of the reconstructed FIB-SEM tomogram. **f**, Evolution of the coverage of the membrane xz cross-section by MOF particles with the inspection depth.**

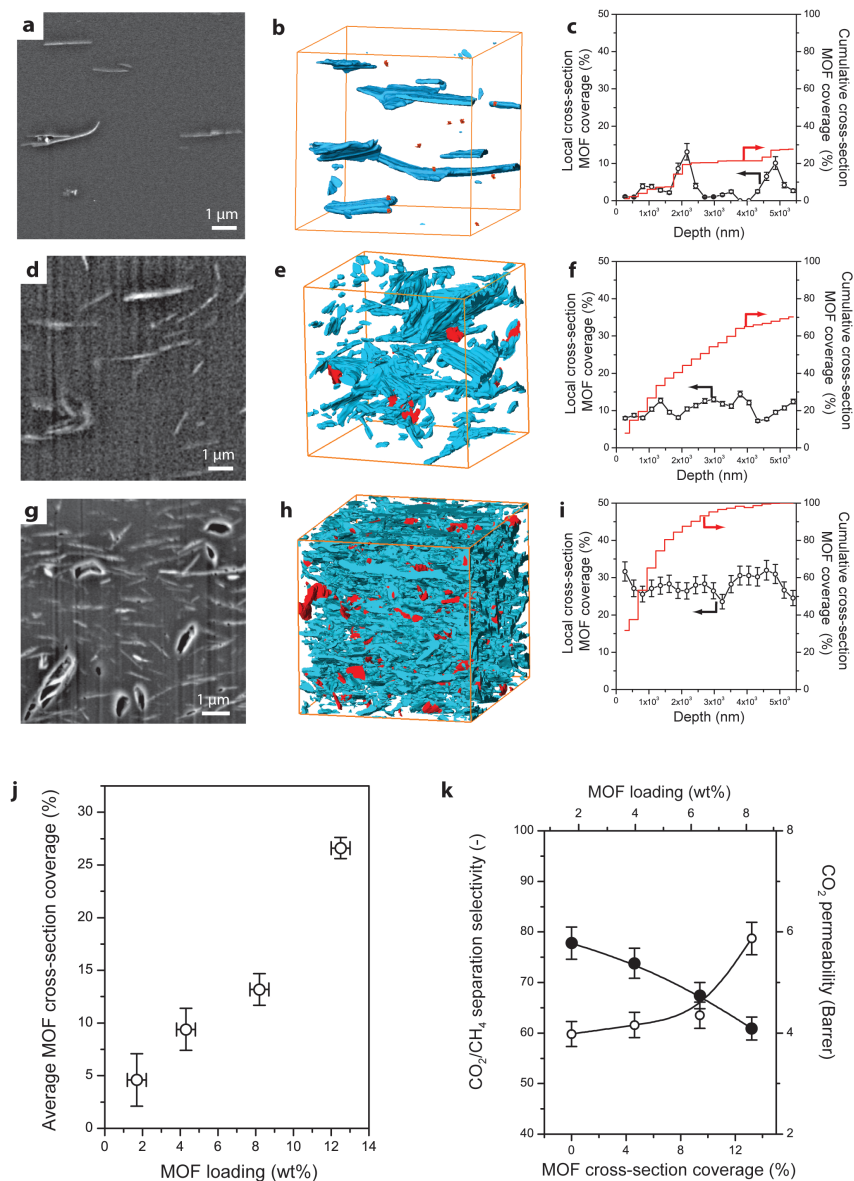


Figure S9: Internal microstructure analysis and separation performance of MOF-polymer composites with varying CuBDC MOF nanosheet loadings. **a,d,g**, SEM micrographs of cross-sections of composite membranes exposed upon FIB milling; **b,e,h**, surface-rendered views of the segmented FIB-SEM tomograms and **c,f,i**, spatial evolution of the coverage of the membrane xz cross-section by MOF filler particles for ns -CuBDC(x)@PI composites with 1.7% (**a-c**), 4.3% (**d-f**), and 12.4% (**g-i**) weight MOF loading, respectively. The corresponding data for a membrane with 8.2 wt% filler loading have been included in Figures 4 and 5 of the main article. Panel **j** depicts the dependence of the average cross-section filler coverage, evaluated over a depth of 5 μm with a discrete step size of 10 voxels (see methods), with the MOF weight loading in the composites. Error bars for filler coverage correspond to the standard error from the analysis of two random regions for ns -CuBDC(2)@PI and ns -CuBDC(12)@PI, and interpolation for the remaining composites. For the TGA-derived MOF loading, error bars correspond to 5% of the full loading range. Panel **k** shows the evolution of the CO₂/CH₄ separation selectivity and the CO₂ permeability ($T=298\text{ K}$, $\Delta P=3\text{ bar}$) with the average filler cross-section coverage. Error bars correspond to the standard error, as determined from three independent tests with selected membranes.

The thin-film casting methodology was successfully extended to prepare *ns*-CuBDC(*x*)@PI composites with varying MOF nanosheet loading in the range of 2-12 wt%. FIB-SEM tomography was also applied to assess and quantify the internal nanostructure of the resulting composite membranes (Fig. S9a-i). The average surface occupation of the membrane cross-section by the MOF nanosheets was found to scale with the filler loading, indicative of the uniform filler spatial distribution (Fig. S9j). The membranes were further studied in gas permeation experiments under standard experimental conditions. For the highest studied filler loading of 12.4 wt%, the membrane showed a significantly higher density of internal defects (voids), which resulted in insufficient mechanical stability to be tested under the above indicated gas permeation conditions. For such MOF filler loading and given the ultrathin nature of the MOF filler crystals, quantification of FIB-SEM tomography results indicated a filler-polymer interface as high as $2 \cdot 10^7 \text{ m}^2/\text{m}^3$. Note that such filler-matrix interface extent is for instance equivalent to that expected for a 73 wt% filler loading in more conventional composites incorporating e.g. 200 nm-sized 3D MOF nanoparticles, and hence expected to pose challenges for the successful integration of both membrane components. Assembly and casting methodologies will require further optimization for very high MOF nanosheet loadings. For the remaining filler loadings, a direct relationship was observed between both the CO₂/CH₄ separation selectivity and the CO₂ permeability with the average cross-section coverage by the MOF nanosheets (Fig. S9k).

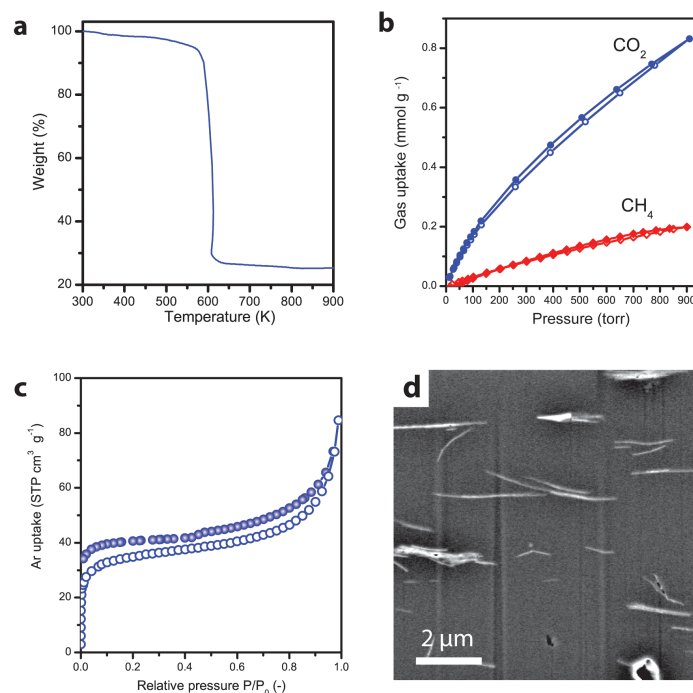


Fig. S10: Synthesis of copper 2,6-naphthalenedicarboxylate MOF nanosheets and the polyimide-based MOF-polymer composite thereof. **a**, Thermogravimetric profile of the Cu(2,6NDC) MOF nanosheets after washing and activation; **b**, CO₂ (blue circles) and CH₄ (red diamonds) sorption isotherms for as-activated Cu(2,6NDC) nanosheets (open symbols correspond to the adsorption branch and closed symbols to the desorption branch); **c**, Argon sorption isotherm at 87 K for as-activated Cu(2,6NDC) nanosheets. Open and full symbols correspond to the adsorption and desorption branches, respectively; **d**, SEM micrograph of a cross-section, exposed upon FIB milling, of a MOF-polymer composite incorporating 8wt% Cu(2,6NDC) MOF nanosheets as fillers within a polyimide matrix. MOF nanosheets are observed as brighter motifs on the gray background corresponding to the polymer matrix.

The MOF nanosheet synthesis method was extended to MOF structures with different linker molecules, as an effective approach to modify the MOF pore size. As shown in Figure 2 (main article), ultrathin nanosheet crystals of Cu(2,6NDC) MOF were successfully synthesized following the three-layer synthesis strategy. Figure S10 summarizes characterization results obtained for the as-activated Cu(2,6NDC) MOF nanosheets and a MOF-polymer composite assembled thereof. CO₂ and CH₄ sorption isotherms demonstrated the preferential adsorption of CO₂ over CH₄ in the Cu(2,6NDC) MOF nanostructure. Argon sorption analysis showed a significant Ar uptake at low relative pressures (<0.05), corresponding to adsorption in the microporous structure of the MOF nanosheets. Similar specific surface areas were determined by Dubinin-Radushkevich analysis of the Ar adsorption isotherm at 87 K (125 m² g⁻¹) and the CO₂ adsorption isotherm at 298 K (165 m² g⁻¹), indicating that the microporous structure of the MOF is equally accessible to both adsorbates. This result contrasts with the effective blockage of Ar from the microporous structure of the activated CuBDC MOFs (Figure 3 in the main article), and demonstrates that the Cu(2,6NDC) MOF nanosheets feature a wider pore aperture, as expected from the bulkier character and the specific orientation of the carboxylate functional groups in the linker molecule^[6]. Cu(2,6NDC) MOF nanosheets were incorporated as filler material in a MOF-polymer composite to assess the impact of the MOF pore aperture size on the gas separation

performance. For the cast composite thin-film, cross-sectional FIB-SEM imaging confirmed the uniform spatial distribution and preferential horizontal orientation of the Cu(2,6NDC) MOF nanosheets within the polymer matrix, therefore effectively exposing their pore system parallel to the gas permeation direction (Fig. S10d). The *ns*-Cu(2,6NDC)(8)@PI membrane was tested in the separation of CO₂ and CH₄ under standard operation conditions (298 K, trans-membrane pressure difference of 3 bar). The results have now been included in the Supplementary Table 1 (6th column). Direct comparison with a composite membrane based on CuBDC MOF nanosheets, with the same filler loading, evidences that a ca. 53% higher CO₂ permeability and a ca. 45% lower CO₂/CH₄ separation selectivity are obtained with the membrane based on Cu(2,6NDC) nanosheets, which is in line with an expected lower restriction to the permeation of both gases through the wider pores of the Cu(2,6NDC) filler material. These results point to the potential to adjust the separation properties of the nanosheet-polymer composites via selection of ultrathin MOF crystals with different pore dimensions or even by preparing composite membranes containing simultaneously two or more types of MOFs in appropriate ratios.

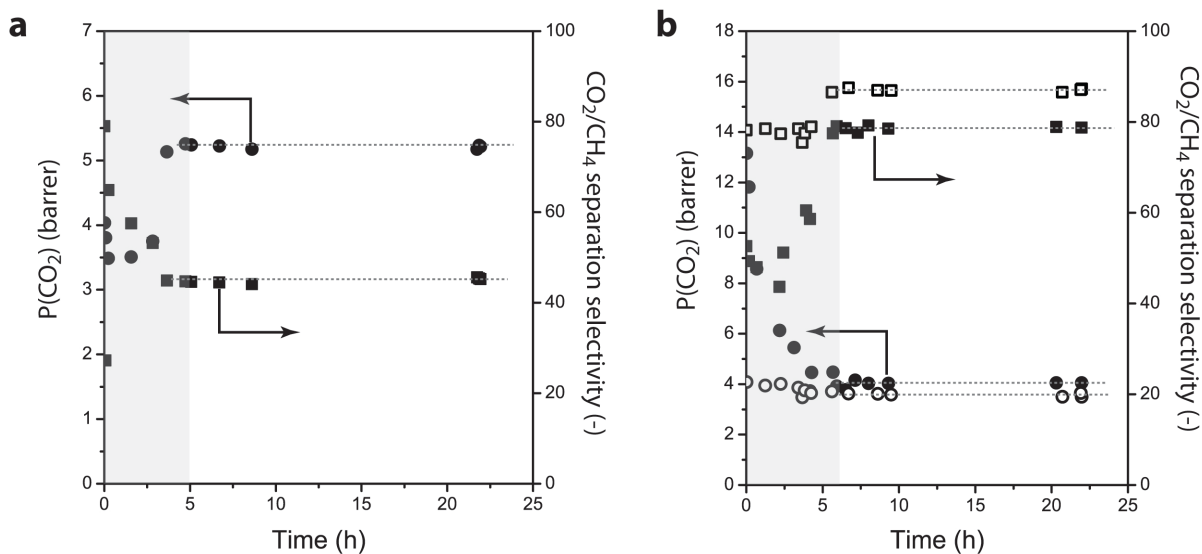


Figure S11: Evolution of the CO₂ permeability (circles) and the CO₂/CH₄ selectivity factor (squares) with time-on-stream during extended gas permeation experiments at 298 K, with *b*-CuBDC(8)@PI (a) and *ns*-CuBDC(8)@PI (b) composite membranes. Full and open symbols correspond to experiments run at trans-membrane pressure differences of 3 and 6 bar, respectively. The shaded regions indicate the transient operation periods. Dotted lines serve as guide to the eye in the steady operation regime.

During the gas permeation experiments, an initial transitory period was observed, during which separation selectivity decreased and gas permeability increased over time. After 4-7 hours of operation, a steady state was reached, and the separation indicators were found to remain constant up to at least 22 hours on-stream. The separation results reported here correspond to the average of five analyses taken after 8 hours of operation, once ensured that the steady state had been reached in all cases.

3. Supplementary Tables.

Table S1. Summary of the gas separation performance obtained with polymer and MOF-polymer composite membranes with different filler loading under several operation conditions.

Membrane	<i>ns</i> -CuBDC(<i>x</i>)@PI			<i>ns</i> -CuBDC(4)@PI	<i>ns</i> -Cu(2,6-NDC)(8)@PI
MOF loading (wt%)	1.7	4.3	8.2	3.7	7.6
Membrane thickness (μm)	52 ± 1^a	45 ± 1	47 ± 1	34 ± 1	55 ± 1
ΔP (bar)	3	3	3	3	3
P_{CO_2} (Barrer) ^b	5.38 ± 0.05	4.74 ± 0.04	4.09 ± 0.01	9.91 ± 0.01	6.28 ± 0.01
P_{CH_4} (Barrer) ^b	0.09 ± 0.00	0.07 ± 0.00	0.05 ± 0.01	0.17 ± 0.02	0.14 ± 0.00
Selectivity (-)	61.6 ± 1.1	63.5 ± 0.8	78.7 ± 1.2	59.5 ± 0.9	43.5 ± 0.4

Table S1 (cont.)

Membrane	PI				<i>b</i> -CuBDC(8)@PI			
MOF loading (wt%)	---				7.9			
Membrane thickness (μm)	45 ± 1				48 ± 1			
ΔP (bar)	3	4.5	6	7.5	3	4.5	6	7.5
P_{CO_2} (Barrer) ^b	5.78 ± 0.02	5.70 ± 0.01	5.48 ± 0.01	5.93 ± 0.01	5.21 ± 0.02	5.63 ± 0.01	4.47 ± 0.02	3.62 ± 0.01
P_{CH_4} (Barrer) ^b	0.10 ± 0.01	0.10 ± 0.01	0.10 ± 0.01	0.12 ± 0.02	0.12 ± 0.01	0.17 ± 0.01	0.30 ± 0.01	0.31 ± 0.01
Selectivity (-)	59.8 ± 0.7	58.3 ± 0.5	52.6 ± 0.5	47.7 ± 0.3	45.0 ± 0.9	34.1 ± 0.8	14.8 ± 0.5	11.8 ± 0.7

Table S1 (cont.)

^a Error corresponds to the standard deviation from 10 different measurements at different locations within each membrane after casting and activation.

^b Error is given as the standard deviation from 5 different analysis in the steady operation state.

Membrane	<i>nc</i> -CuBDC(8)@PI				<i>ns</i> -CuBDC(8)@PI			
MOF loading (wt%)	8.3				8.2			
Membrane thickness (μm)	51 ± 1				47 ± 1			
ΔP (bar)	3	4.5	6	7.5	3	4.5	6	7.5
P_{CO_2} (Barrer) ^b	5.03 ± 0.01	4.93 ± 0.01	4.03 ± 0.01	3.83 ± 0.01	4.09 ± 0.01	3.73 ± 0.02	3.59 ± 0.01	2.78 ± 0.02
P_{CH_4} (Barrer) ^b	0.10 ± 0.00	0.10 ± 0.00	0.10 ± 0.00	0.11 ± 0.00	0.05 ± 0.01	0.05 ± 0.01	0.04 ± 0.01	0.03 ± 0.01
Selectivity (-)	49.4 ± 0.9	48.8 ± 1.6	42.0 ± 0.6	34.8 ± 0.5	78.7 ± 1.2	79.2 ± 0.7	87.1 ± 0.5	88.2 ± 1.3

4. Supplementary Videos.

Videos S1-S2. Reconstructed FIB-SEM tomograms of the internal structure of MOF-polymer composite materials.

The videos show the sequence of aligned SEM micrographs through the FIB-SEM tomograms for membranes cast out of the *b*-CuBDC@PI and *ns*-CuBDC@PI MOF-composite materials. CuBDC MOF particles are perceived as brighter motifs on the dark grey background corresponding to the polyimide matrix. Internal voids in the membrane appear black. SuppVideo_1, corresponding to the *b*-CuBDC(8)@PI composite material, shows relatively large, mostly cubic-shaped MOF crystals within the polymer matrix. In contrast, SuppVideo_2 shows the presence of a much higher number of very thin MOF nanosheets very evenly distributed over the examined volume for the *ns*-CuBDC(8)@PI composite.

Video designation	Composite material designation	File type/size (MB)
SuppVideo_1	<i>b</i> -CuBDC@PI	QuickTime movie /19.0 MB
SuppVideo_2	<i>ns</i> -CuBDC@PI	QuickTime movie /18.3 MB

Supplementary references

- ¹ Carson, C. G., et al. Synthesis and structure characterization of copper terephthalate metal-organic framework. *Eur. J. Inorg. Chem.* 2338-2343 (2009).
- ² Zornoza, B., et al. Functionalized flexible MOFs as fillers in mixed matrix membranes for highly selective separation of CO₂ from CH₄ at elevated pressures. *Chem Commun.* **47**, 9522-9524 (2011).
- ³ Carson, C. G., et al. Structure solution from powder diffraction of copper 1,4-benzenedicarboxylate. *Eur. J. Inorg. Chem.* 2140-2145 (2014).
- ⁴ Gascon, J., Aguado, S., Kapteijn, F. Manufacture of dense coatings of Cu₃(BTC)₂ (HKUST-1) on α -alumina. *Micropor. Mesopor. Mater.* **113**, 132-138 (2008).
- ⁵ Chui, S. S. Y., Lo, S. M.-F., Charmant, J. P. H., Orpen, A. G., Williams, I. D. A chemically functionalizable nanoporous material [Cu(TMA)₂(H₂O)₃]_n. *Science* **283**, 1148-1150 (1999).
- ⁶ Eddaoudi, et al. Systematic design of pore size and functionality in isorecticular MOFs and their application in methane storage. *Science* **295**, 469-472 (2002).